J. Phys. Chem. A **2000,** *104,* 6218−6226

# Photochemical Kinetics of Vibrationally Excited Ozone Produced in the 248 nm Photolysis of $O_2/O_3$ Mixtures

**Jack G. Green,[†] Jichun Shi,[‡,§] and John R. Barker[†,‡,*]**

*Department of Chemistry and Department of Atmospheric, Oceanic, and Space Sciences,*
*University of Michigan, Ann Arbor, Michigan 48109-2143*

*Received: February 17, 2000; In Final Form: April 25, 2000*

Infrared emission from vibrationally excited ozone was monitored as a function of time following pulsed laser photolysis of $O_3/O_2$ mixtures with total pressures from 300 to 1800 Torr at 295 K. The emission data obtained at 9.6 $\mu$m were analyzed by nonlinear least squares and by constructing $\chi^2$ surfaces. The results are entirely consistent with a conventional mechanism that includes the following reactions: (1a) $O_3 + h\nu \rightarrow O(^1D) + O_2(a^1\Delta)$; (1b) $O_3 + h\nu \rightarrow O(^3P) + O_2$; (2a) $O(^1D) + O_2 \rightarrow O(^3P) + O_2(^1\Sigma_g{}^+)$; (2b) $O(^1D) + O_2 \rightarrow O(^3P) + O_2$; (3) $O(^3P) + O_2 + O_2 \rightarrow O_3(v) + O_2$; (4) $O_3(v) + O_2 \rightarrow O_3 + O_2$; (5a) $O_2(^1\Sigma_g{}^+) + O_3 \rightarrow O + O_2 + O_2$; (5b) $O_2(^1\Sigma_g{}^+) + O_3 \rightarrow O_3(v) + O_2$; (6) $O_2(^1\Sigma_g{}^+) + O_2 \rightarrow O_2 + O_2$. There is no evidence for participation by ozone excited electronic states, but the reaction time scales are not well separated, leading to complexities in the analysis. The measured rate constants $k_3$ $(\pm\sigma) = (6.0 \pm 1.1) \times 10^{-34}$ cm$^6$ s$^{-1}$ and $k_5$ $(\pm\sigma) = (2.26 \pm 0.15) \times 10^{-11}$ cm$^3$ s$^{-1}$ are in good agreement with literature values. The phenomenological rate constant $k_4$ $(\pm\sigma) = (1.2 \pm 0.2) \times 10^{-11}$ cm$^3$ s$^{-1}$ is consistent with a model for vibrational deactivation. The measured value for the ratio $k_{1a}k_{2a}/(k_1k_2) = 0.86 \pm 0.13$ is combined with a literature value for $k_{1a}/k_1$ to give an improved estimate for $k_{2a}/k_2 = 0.95$ (+0.05/−0.13).

## Introduction

The ozone Hartley band, which is centered near 250 nm, and Huggins band, a long wavelength extension of the Hartley band, are responsible for shielding the earth's surface from harmful ultraviolet light. Ozone is formed by the $O + O_2$ recombination reaction, which has been the subject of many studies.[1−4] Under atmospheric conditions, this reaction is third-order, and excellent agreement exists among the reported rate constants. However, the kinetics are more complex at higher pressures. For example, recombination rate constants at about 400 Torr of $O_2$ were found by previous researchers[5−8] to be considerably smaller than at lower pressures, a behavior attributed to the participation of a weakly bound electronic state of $O_3$. Hippler et al.[9] reported an anomalous pressure dependence in measurements that ranged from 1 to 1000 bar of $N_2$, Ar, and He. They attributed the anomaly to the participation of collisional complexes and/or weakly bound ozone electronic states. Shi and Barker,[10] who used infrared emission to monitor the reaction, also found deviations from third-order kinetics. One motivation for the present work was to identify the cause of the anomalous reaction kinetics.

A second motivation for the present work was to investigate the deactivation of vibrationally excited ozone ($O_3(v)$) produced via the $O + O_2$ recombination reaction.[11−13] In the lower atmosphere, collisional activation and deactivation maintain a Boltzmann distribution characterized by the local translational temperature. This state of equilibrium characterized by the local temperature is termed "local thermodynamic equilibrium" (LTE). In the mesosphere and above (>70 km), the collision frequency is much lower and spontaneous infrared emission from the strong transitions in ozone competes successfully with collisional deactivation and contributes to the infrared air glow.[14] Because in general the radiation temperature in the atmosphere is not equal to the local translational temperature, the resulting steady-state vibrational distribution is not equal to the Boltzmann distribution and a state of "non-LTE" exists.[15−18] Non-LTE influences the energy budget of the upper atmosphere and it affects the ability to use infrared emission observations from satellites to extract information about the abundance of ozone at high altitudes.[19−21]

A third motivation for the present work was to investigate the chemical kinetics of excited electronic states of $O_2$. The Hartley band photolysis of ozone produces $O(^1D)$, which is quenched by $O_2$ to produce $O_2(^1\Sigma_g{}^+)$. This is the principal atmospheric source of $O_2(^1\Sigma_g{}^+)$.[22] Emissions from $O(^1D)$ and $O_2(^1\Sigma_g{}^+)$ contribute to upper atmospheric air glow, which can be observed and interpreted to deduce species concentrations[22] and atmospheric dynamics.[23] In particular, the $b^1\Sigma_g{}^+ \rightarrow X^3\Sigma_g{}^-$ band (the atmospheric band) can be used to deduce ozone concentrations, if the $O_2(^1\Sigma_g{}^+)$ production efficiency is known for the energy transfer between $O(^1D)$ and $O_2$. The most prominent emission (762 nm) in this same band system has often been used for laboratory studies of $O_2(^1\Sigma_g{}^+)$ quenching.[2,24]

In the present work, the production and loss of $O_3(v)$ were investigated at $O_2$ pressures of up to 1800 Torr of $O_2$ (at $T \approx$ 295 K) via time-resolved infrared fluorescence (IRF) monitored at wavelengths near 3.4, 4.7, and 9.6 $\mu$m. These emissions correspond to various vibrational transitions of the $O_3(v)$ vibrational intermediates. We show that the infrared emission data obtained at 9.6 $\mu$m using a fast semiconductor detector can be explained without invoking excited electronic states of ozone and that the anomalous pressure dependence reported

---

[†] Department of Chemistry.

[‡] Department of Atmospheric, Oceanic, and Space Sciences.

[§] Present address: Proctor & Gamble Co., Ivorydale Technical Center, 5299 Spring Grove Avenue, Cincinatti, OH 45217-1078.

[*] Corresponding author (E-mail: jrbarker@umich.edu).

10.1021/jp000635k CCC: $19.00

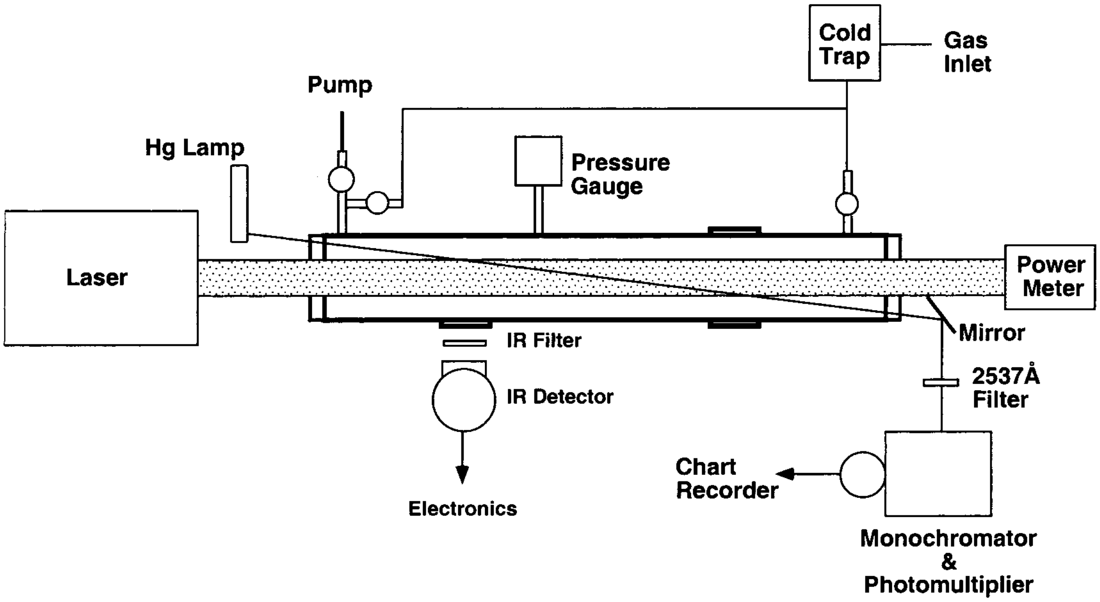

**Figure 1.** Schematic of experimental apparatus.

earlier[10] was due to the effect of experimental noise on the nonlinear least-squares analysis. We obtain only limited information about the vibrational deactivation of $O_3(v)$, but we obtain an improved estimate of the branching ratio for production of $O_2(^1\Sigma_g^+)$ in collisions of $O(^1D)$ with $O_2$. In the following sections, we present the experimental details, chemical mechanism, instrument response function, statistical analysis, and results, followed by discussion.

## Experimental Section

The experimental apparatus (Figure 1) consisted of a cell with two light beams passing down the long axis, a detection system for each beam, and an infrared detector perpendicular to the cell. The cell was a well-passivated 48 cm long × 3.8 cm diameter stainless steel tube fitted with Suprasil end windows and a magnesium fluoride side window; two additional Suprasil side windows were used occasionally for monitoring the ozone concentration. Ozone-resistant silicone rubber O-rings were used to seal the windows. The photolysis laser beam, which was directed down the long axis of the cell, was generated by a Lumonics pulsed excimer laser (HyperEx-400) operating at the KrF (248 nm) transition. The photolysis laser beam diameter was 1.5−2.5 cm and the pulse energy was ∼80 mJ/pulse, as monitored with a calibrated volume-absorbing power meter (Scientech model no. 380103). Typical pulse lengths were 10−20 ns and the pulse repetition frequency was typically 10−25 Hz.

Infrared fluorescence at wavelengths shorter than 5.5 $\mu$m was monitored perpendicular to the laser beam in real time by a liquid nitrogen cooled InSb semiconductor detector (InfraRed Associates, Inc.) with a nominal response time of ∼1.5 $\mu$s. We designated this detector INSB-1. Infrared fluorescence at wavelengths greater than ∼5.5 $\mu$m was observed with either of two HgCdTe semiconductor detectors (Infrared Associates). The HgCdTe detector (4 mm × 4 mm) which we designate HCT-1 had a time response of ∼2 $\mu$s and was used only as part of the wavelength survey. The second HgCdTe detector (model number HCT-50), which we designate HCT-2, had a much faster time response (∼0.5 $\mu$s, see below) and was used for the kinetics measurements. The detector signals were amplified using a matched preamplifier (Perry). Signals from detectors HCT-1 and INSB-1 were amplified again using a Tektronix model AM-502 differential amplifier. The signals were sent to a digital oscilloscope (LeCroy 9400) where 5000 to 50 000 laser shots were averaged per experiment. The time response of HCT-2 was characterized (as described below) by using a silicon photodiode (Thorlabs DET 100) with a 10 ns rise time and a red light-emitting diode driven by a 50 MHz pulse generator (WaveTek model 801).

Infrared emission from the three bands was isolated by broad-band interference filters, which also blocked stray laser light. The 3.4 $\mu$m filter has a half width of ∼0.2 $\mu$m with an average transmittance of 85%. The 4.7 $\mu$m filter is a 4 $\mu$m long-pass filter (∼60% average transmittance), but due to the cutoff of the InSb detector, only emission in the 4.0−5.5 $\mu$m region was captured by the detector. The 9.6 $\mu$m filter is a 9 $\mu$m long-pass filter (∼50% average transmittance). Again, emission only in the 9−14 $\mu$m region was captured by the detector due to the cutoff by the HgCdTe detector. Transmission spectra of all the infrared filters were measured by an FTIR spectrometer (Nicolet DX V4.56).

The oxygen gas used in these experiments was 99.995% pure with less than 1 ppm of $H_2O$ (Air Products). Ozone was produced by a home-built silent ozonizer and was flowed through the cell at a volume flow rate of <10 scc/sec. Tests showed that there was no measurable difference in experiments with much higher or much lower flow rates. In some experiments a cold trap was used on the gas inlet lines, but the results were not affected by the use of the cold trap.

Total pressure in the cell was measured using a capacitance manometer (Baratron, 10 000 Torr full scale). The ozone concentration was monitored continuously by 253.7 nm light from a low-pressure mercury vapor pen lamp (Oriel) that was counter-propagated down the long axis of the cell at a small angle to the laser beam. The attenuation of this light beam was monitored with a detection system consisting of a narrow-band interference filter, followed by a 1/4 m monochromator (Jarrell-Ash) and photomultiplier (Hamamatsu). The photomultiplier signal was amplified with a preamplifier (Tektronix AM502) and recorded using a strip chart recorder. We estimate that the measurement error of the $O_3$ concentration is of the order of ±5%.

In carrying out a typical experiment, the gas flow was established and the ozonizer was energized. After the ozone concentration had stabilized, the laser was operated and the infrared emission data were acquired and summed (for signal/noise improvement) using the digital oscilloscope. At the end of the experimental run, the data were transferred to a computer and stored for subsequent analysis.

## Results and Data Analysis

**Identification of Emission Bands.** Four infrared emission features were observed previously in this laboratory from $O_3(v)$ produced via the $O + O_2$ recombination reaction: 9.6, 4.7, 3.4, and 2.1−2.7 $\mu$m. The 2.1−2.7 $\mu$m emission is not considered in the present work because of its low intensity. A fifth emission band observed near 1.9 $\mu$m was hypothesized to originate from an ozone-excited electronic state, but it was subsequently identified by Fink et al.[54] as the collision-induced Noxon band $b^1\Sigma_g^+ \rightarrow a^1\Delta_g$ transition in $O_2$ and is not associated with ozone. Emissions in the range of 6−8 $\mu$m were reported by von Rosenberg and Trainor,[7,8] but we were not able to detect any emissions in this spectral region, despite extensive efforts. Rawlins and Armstrong[12] also were unable to observe emissions in this region. Other spectroscopic studies[25,26] have reported that none of the ozone-excited electronic states is thermally accessible in the recombination reaction.

The four infrared emission bands can all be attributed to vibrationally excited $O_3(v)$ intermediates formed in the $O + O_2$ recombination reaction. The three vibrations of $O_3$ have frequencies of 1103, 701, and 1042 cm$^{-1}$, respectively.[27,28] The 9.6 $\mu$m emission is part of the $O_3$ asymmetric stretch ($\nu_3$) 1042 cm$^{-1}$ fundamental and includes contributions from transitions of the following three types:[28−30]

9.6 $\mu$m:

$$(\nu_1\ \nu_2\ \nu_3) \rightarrow (\nu_1\ \nu_2\ \nu_3 - 1)$$

$$(\nu_1\ \nu_2\ \nu_3) \rightarrow (\nu_1 + 1\ \nu_2\ \nu_3 - 2)$$

$$(\nu_1\ \nu_2\ \nu_3) \rightarrow (\nu_1 - 1\ \nu_2\ \nu_3)$$

Most of the oscillator strength is associated with the asymmetric stretch ($\nu_3$) and thus the first transition type is much stronger than the other two. In the 4.7 $\mu$m region, three types of $O_3(v)$ vibrational transitions are possible:

4.7 $\mu$m:

$$(\nu_1\ \nu_2\ \nu_3) \rightarrow (\nu_1 - 1\ \nu_2\ \nu_3 - 1)$$

$$(\nu_1\ \nu_2\ \nu_3) \rightarrow (\nu_1\ \nu_2\ \nu_3 - 2)$$

$$(\nu_1\ \nu_2\ \nu_3) \rightarrow (\nu_1 - 2\ \nu_2\ \nu_3)$$

Only the first of these is important, however, because the other two transition types have very small Einstein coefficients.[28] Similarly, three types of transitions are possible in the 3.4 $\mu$m region:

3.4 $\mu$m:

$$(\nu_1\ \nu_2\ \nu_3) \rightarrow (\nu_1\ \nu_2\ \nu_3 - 3)$$

$$(\nu_1\ \nu_2\ \nu_3) \rightarrow (\nu_1 - 1\ \nu_2\ \nu_3 - 2)$$

$$(\nu_1\ \nu_2\ \nu_3) \rightarrow (\nu_1 - 2\ \nu_2\ \nu_3 - 1)$$

Again, the first of these has much larger Einstein coefficients than the other two. Emission in the 2.1−2.7 $\mu$m region is likely due to combination band transitions of highly vibrationally excited $O_3(v)$.

A survey of the rates of production and loss was carried out at 3.4, 4.7, and 9.6 $\mu$m; some results obtained with the detector HCT-2 are shown in Figure 2, where at least three time constants are apparent in each IRF decay measurement. The rise time corresponds to the fastest process, the first decaying portion corresponds to the second fastest process, etc. In the survey experiments, the data were limited by the slow time response of the detectors designated INSB and HCT-1, and the rise time could not be obtained reliably. However, the first decaying portion of the IRF could be obtained with sufficient accuracy at each wavelength to show that the rate constants ($k_{\mathrm{decay}}$) are similar at all three wavelengths (Figure 3). The data in Figure 3, which have been published previously,[10] are consistent with the hypothesis that all of these emissions originate from $O_3(v)$. Because the infrared detector designated HCT-2 has the fastest time response and therefore affects the data analysis least, only the data obtained with HCT-2 at 9.6 $\mu$m were analyzed quantitatively, as described in the following sections.

**Chemical Mechanism.** The following mechanism explains all of the 9.6 $\mu$m measurements obtained using detector HCT-2:

$$O_3 + h\nu \rightarrow O(^1D) + O_2(a^1\Delta) \tag{1a}$$

$$\rightarrow O(^3P) + O_2 \tag{1b}$$

$$O(^1D) + O_2 \rightarrow O(^3P) + O_2(^1\Sigma_g^+) \tag{2a}$$

$$\rightarrow O(^3P) + O_2 \tag{2b}$$

$$O(^3P) + O_2 + O_2 \rightarrow O_3(v) + O_2 \tag{3}$$

$$O_3(v) + O_2 \rightarrow O_3 + O_2 \tag{4}$$

$$O_2(^1\Sigma_g^+) + O_3 \rightarrow O + O_2 + O_2 \tag{5a}$$

$$\rightarrow O_3(v) + O_2 \tag{5b}$$

$$O_2(^1\Sigma_g^+) + O_2 \rightarrow O_2 + O_2 \tag{6}$$

where O, $O_2$, and $O_3$ are in their ground electronic states ($^3P$, $X^3\Sigma_g^-$, and $^1A_1$, respectively) unless otherwise indicated.

In the present system, ozone is the only significant absorber; absorption by $O_2$ at 248 nm is very small and can be neglected.[31−34] The photolysis of $O_3$ is well known to proceed by the two pathways in reaction 1 and the branching ratio is $k_{1a}/k_1 = 0.91 \pm 0.03$ at 248 nm.[35] The $O(^1D)$ produced in the photodissociation reacts very quickly with the abundant $O_2$. At the lowest pressures reported here (300 Torr), the time constant for loss of $O(^1D)$ is $\tau \approx 3$ ns, based on the accepted value for rate constant $k_2$.[2] This time constant is much shorter than the infrared detector response and, for the purpose of data analysis, is assumed to be instantaneous. One of our objectives is the measurement of the branching ratio for reaction 2, which is not known with great accuracy.

Reaction 3 is well known from experimental studies at low pressure.[1,2] At pressures of the order of several hundred bar, 2 orders of magnitude greater than in the present work, the rate constant $k_3$ exhibits falloff behavior that may signal the effects of the energy transfer mechanism and/or the presence of ozone excited electronic states.[9]

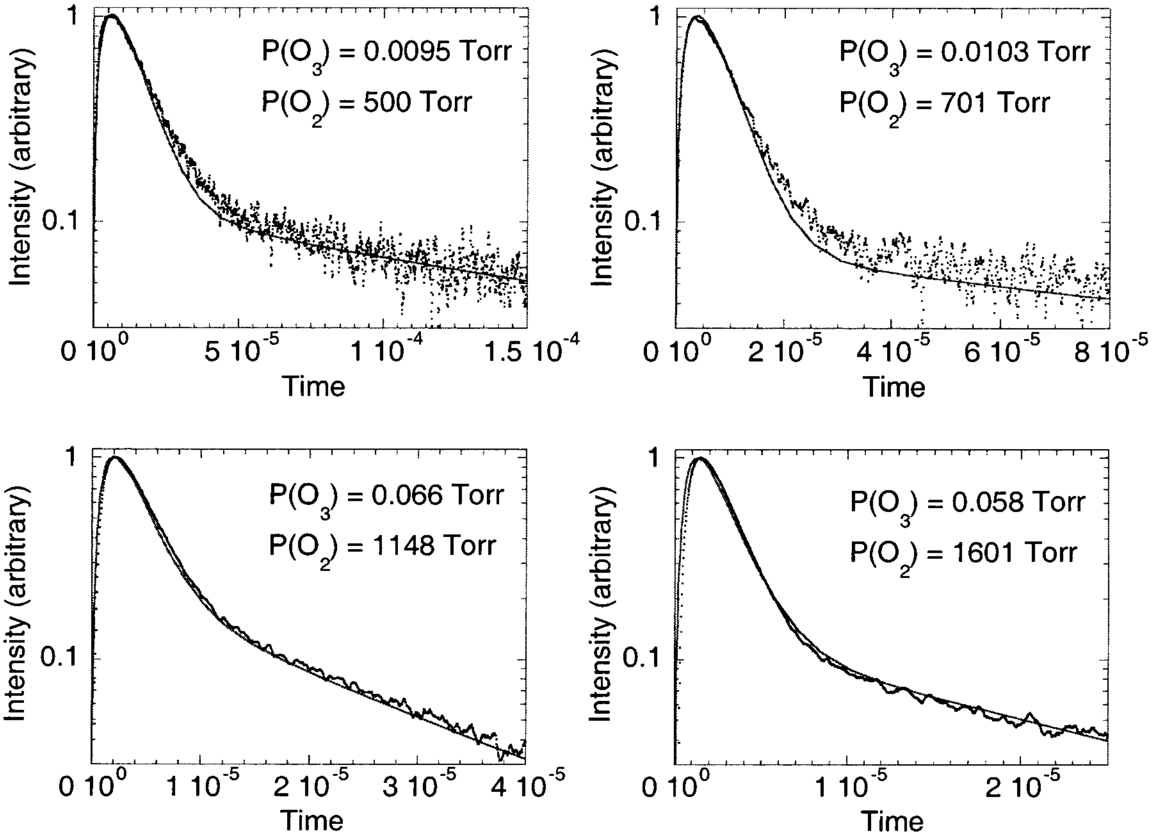

**Figure 2.** Representative experimental data obtained at 9.6 $\mu$m (with detector HCT-2). The solid lines are from the global $\chi^2$ analysis described in the text.

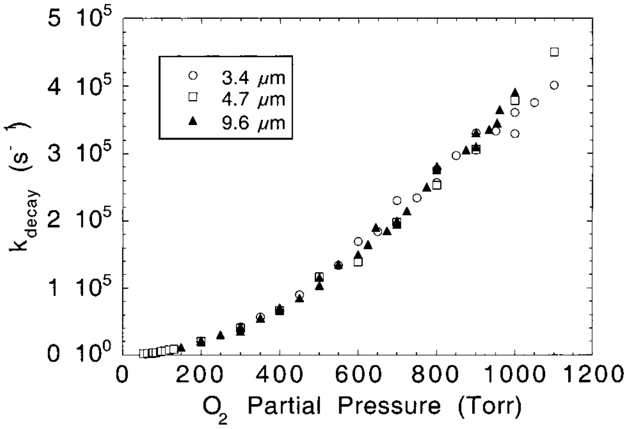

**Figure 3.** Survey of decay rate constants[10,46] obtained with detectors INSB and HCT-1 at three wavelengths.

Reaction 4 represents the deactivation of vibrationally excited ozone, $O_3$(v), while neglecting the details of the process. There are more than 250 bound vibrational states of $O_3$ and the recombination reaction produces $O_3$(v) in an unknown initial distribution. The actual process of vibrational deactivation requires many collisions and is extremely complex.[11−13,36] Fortunately, a single phenomenological bimolecular rate constant representing vibrational deactivation is sufficient for present purposes, because most of the vibrational deactivation is very rapid compared to a bottleneck low on the vibrational energy ladder.[37−39]

Reactions 5 and 6 are the routes by which $O_2(^1\Sigma_g^+)$ is quenched. From measurements carried out by monitoring the forbidden $b^1\Sigma_g^+ \rightarrow X^3\Sigma_g^-$ transition of $O_2$ at 762 nm, the rate constants are reasonably well known.[1,2,24] In the present work, a new independent measurement of $k_5$ is reported that is in good agreement with previous work. The $k_{5a}/k_5$ branching ratio is not as well known, but the present experiment is not sensitive to this quantity, as is shown below.

This is the conventional mechanism for this chemical system. Although it was concluded by Shi and Barker[10] that excited electronic states of ozone are produced in this system, we have used a faster infrared detector in the present work and have found that the conventional mechanism describes the results accurately without the need for invoking participation by ozone-excited electronic states.

An analytical solution for the time-dependent concentration of $O_3$(v) was obtained by adopting the pseudo-first-order approximation and assuming the $O_2$ and $O_3$ concentrations do not change with time. For $O_2$, this assumption is excellent, because $[O_2]_0 \gg [O_3]_0$. For $O_3$, this assumption is less accurate, because 5−10% of the ozone was photodissociated initially in the experiments. The ozone concentration variation is most relevant to reaction 5, which, however, has a very long time constant (due to the use of low $O_3$ concentrations). The long time constant allows the ozone concentration ample time to recover following the laser pulse and thus the fluctuation in $O_3$ concentration has little effect. The analytical expression for $[O_3(v)]$ was obtained by solving the differential equations (subject to the approximations described above) and can be written conveniently as follows:

$$[O_3(v)] = \frac{k_3[O_2]_0^2[O]_0 + \beta}{k_4[O_2]_0 - k_3[O_2]_0^2}\{\exp(-k_3[O_2]_0^2 t) - \exp(-k_4[O_2]_0 t)\} + \frac{k_{5b}[O_3]_0[O_2^*]_0 - \beta}{k_4[O_2]_0 - \alpha}\{\exp(-\alpha t) - \exp(-k_4[O_2]_0 t)\} \quad (7a)$$

where $O_2^*$ designates $O_2(^1\Sigma_g^+)$.

$$\alpha = k_5[O_3]_0 + k_6[O_2]_0 \tag{7b}$$

$$\beta = \frac{k_{5a}k_3[M][O_2]_0[O_3]_0[O_2^*]_0}{k_5[O_3]_0 + k_6[O_2]_0 - k_3[O_2]_0^2} \tag{7c}$$

Note that each exponential term can be written:

$$T = B\exp[-kt] \tag{8}$$

where $B$ is independent of time and $k$ is a pseudo-first-order rate constant.

There are three time constants associated with the expression for $[O_3(v)]$ and with the experimental data, and four processes are responsible: the recombination reaction 3, the vibrational deactivation reaction 4, and reactions 5 and 6 for loss of $O_2(^1\Sigma_g^+)$, and the instrument response. Before it is possible to use these expressions for analyzing the data, it is necessary to consider the effects of a fourth time constant: the instrument response function.

**Instrument Response Function.** The time response of the HgCdTe semiconductor detector–preamplifier (HCT-2) used in this work is only moderately fast, depends somewhat on signal amplitude, and is nonexponential. Because the HCT-2 time response is only moderately fast, the frequency of the detected signals is somewhat limited and deconvolution of the detector response becomes necessary. The HCT-2 was characterized by measuring the detector response to "square wave" light pulses.

Light pulses were generated using a fast square wave voltage pulse generator to drive a red light-emitting diode (LED). Detector HCT-2 is sensitive to a broad range of wavelengths from the visible to beyond 10 $\mu$m and thus could detect the LED emission. The light pulse emitted by the LED was monitored using a silicon photodiode detector (PDD) that has a 10 ns rise time. To characterize HCT-2, the LED was set up so that it could be viewed simultaneously by both detectors and the signals were recorded using the digital oscilloscope. We assumed that the PDD output signal is proportional to the LED emitted light intensity and simulated the measured HCT-2 output by convoluting various assumed HCT-2 response functions with the measured exponential behavior of the PDD output.

By trial-and-error, we found that the HCT-2 instrument response is described with reasonable accuracy by the following function:

$$g(t) = Au(t - \Delta_{ir})\exp[-a^2(t - \Delta_{ir})^2] \tag{9}$$

where $g(t)$ is the instrument response function, $A$ is a proportionality constant, $a$ is a parameter describing the time response, $\Delta_{ir}$ is a short delay time (0.17 $\mu$s), and $u(t - \Delta_{ir})$ is the unit step function. This function is merely a convenient empirical representation of the instrument response; the individual parameters have no particular physical significance.

It is likely that a good representation of the instrument response could also be constructed from a sum of terms that consist of an exponential multiplied by $t^n$, as expected from a linear circuit analysis, but we did not investigate that possibility. A single exponential with a short time delay gives an adequate representation, but not as good as that given by eq 9. By varying the LED intensity, we found that the parameter $a$ in eq 9 decreased systematically by about 25% for initial signal amplitudes that produced voltage outputs from the matched preamplifier of 1.4–20 mV. In the $O_3$ emission experiments, the maximum signal amplitudes fell in a much smaller range, producing the corresponding average value of $a = 2.25 \times 10^6$ s$^{-1}$ with a maximum variation of 10%. For each individual experimental run in the following data analysis, we used the value for parameter $a$ that corresponded to the initial intensity and neglected the weak detector nonlinearity when carrying out the convolution. Although not perfect, eq 9 gives a better representation than a single exponential and its convenient Laplace transform facilitates data analysis. As shown below, the rate constants derived from this work by using this procedure are in good agreement with literature values, showing that the weak nonlinearity does not pose a significant problem.

Each exponential term that appears in the expression for $[O_3(v)]$ ( eq 7) can be convoluted with $g(t)$, which, as mentioned above, has a convenient Laplace transform:

$$I(t) = \int_0^t f(t-\tau)\, g(\tau)\, d\tau = \int_0^t Be^{-k(t-\tau)}Ae^{-a^2(\tau-\Delta_{ir})^2} d\tau \tag{10a}$$

$$I(t) = AB\frac{\sqrt{\pi}}{2a}\exp\left[-k(t - \Delta_{ir}) + \frac{k^2}{4a^2}\right] \times \left\{\operatorname{erf}\left[\frac{k}{2a}\right] - \operatorname{erf}\left[\frac{k}{2a} - (t - \Delta_{ir})\right]\right\} \tag{10b}$$

where $I(t)$ is the time-dependent IRF intensity, $A$ is the proportionality factor which relates the measured IRF intensity to $[O_3(v)]$, $B$ is the preexponential factor, $k$ is the pseudo-first-order rate constant for the reaction, erf(x) is the error function with argument $x$, and the other constants and variables are as defined above. The resulting expression is rather messy, but easily computed, and it incorporates the full chemical mechanism and the effects of instrument response.

**Statistical Analysis of 9.6 *μ*m Data.** Using detector HCT-2 at 9.6 $\mu$m, we carried out 43 experiments at room temperature (~295 K) over the range of pressures from 300 to 1800 Torr. The data analysis of the three time constants apparent in Figure 2 is complicated, because of the influence of the instrument response and because the relative ordering of the rates associated with several processes varies with $O_2$ pressure. A full statistical analysis of the IRF data using the mechanism described above would require fitting eight parameters: $[O]_0$, $[O_2^*]_0$, $k_3$, $k_4$, $k_{5b}$, $k_5$, $k_6$, and amplitude factor $A$. Note that the initial concentrations of O-atoms and $O_2^*$ depend on the amount of $O_3$ that is photolyzed and on the following ratio:

$$\frac{[O_2^*]}{[O]_0} = \frac{k_{1a}}{k_1}\frac{k_{2a}}{k_2} = B_1B_2 \tag{11}$$

where $B_1$ and $B_2$ are branching ratios. Least-squares fitting can find the product $B_1B_2$, but not the individual values. Furthermore, note that the relative values of $k_{5b}$ and $k_5$ can be written in terms of branching ratio $B_5$:

$$\frac{k_{5b}}{k_5} = 1 - \frac{k_{5a}}{k_5} = 1 - B_5 \tag{12}$$

Both branches of reaction 5 result in formation of $O_3(v)$: reaction 5b forms $O_3(v)$ directly and the O-atom formed in reaction 5a reacts very rapidly (compared to the time constant of reaction 5) via reaction 3 to produce $O_3(v)$. Thus, the two branches of reaction 5 are virtually indistinguishable for the present reaction conditions and the IRF data are not expected to be sensitive to branching ratio $B_5$. This lack of sensitivity was confirmed by the experiments, as discussed further below.

**Least Squares Analysis.** The nonlinear least-squares analyses reported here were carried out using the Levenberg–Marquardt

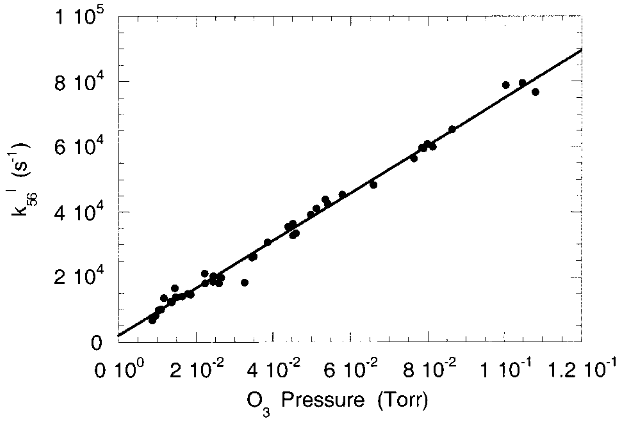

**Figure 4.** Pseudo-first-order rate constant $k_{56}{}^{I}$ vs ozone partial pressure.

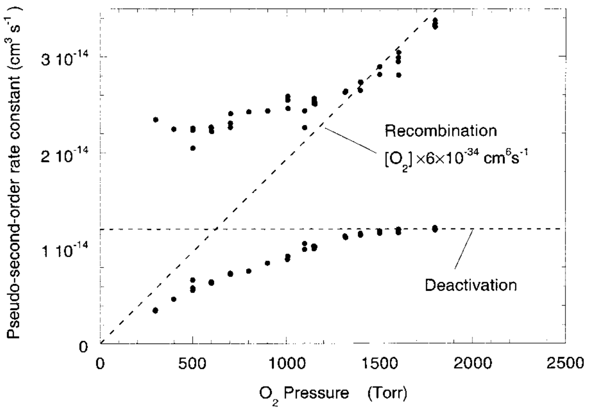

**Figure 5.** Nonlinear least-squares results that show the effects of correlations. See text for details.

algorithm described by Bevington.[40] The IRF data shown in Figure 2 are typical. At every pressure investigated, the IRF intensity rises very rapidly (with time constant greater than four times the detector time constant), decays relatively quickly, and then decays further on a significantly longer time scale. The solid lines shown in the figure are calculated using the parameters corresponding to the minimum $\chi^2$ described below for the total of *all* experimental runs. They are *not* least-squares fits of these individual experiments taken one at a time.

A full unconstrained fit of the data did not lead to useful results, but we found that the data can be fitted quite accurately, as in previous work,[10] by neglecting the effects of the detector time response and adopting an expression consisting of the sum of three exponential terms, each characterized by a pseudo-first-order rate constant $k_i{}^{I}$. The experiments were designed so that reaction 5 is slower than reactions 3 and 4, and reaction 6 is almost negligible under all of the conditions investigated. Therefore, it is easy to identify the slowest decay, characterized by pseudo-first-order rate constant $k_{56}{}^{I}$, with the slowest reactions: reactions 5 and 6. A plot of $k_{56}{}^{I}$ vs ozone partial pressure for all of the runs is shown in Figure 4. The slope of the straight line can be identified with bimolecular rate constant $k_5 = (2.26 \pm 0.04) \times 10^{-11}$ cm$^3$ s$^{-1}$ and the intercept can be identified with the average pseudo-first-order rate constant for reaction 6. We did not attempt to extract the bimolecular rate constant for reaction 6.

The value obtained for rate constant $k_5$ is in excellent agreement with literature values,[1,2,24] despite the simplicity of this analysis. This was possible because the pseudo-first-order rate constant $k_5{}^{I}$ is much slower than both the detector time response and the other two pseudo-first-order rate constants. It is not affected significantly by the initial depletion of $O_3$ from the photolysis laser, because on the long time scale of reaction 5 the depleted ozone has been restored: most of the atomic oxygen produced by the laser pulse has recombined via reaction 3 and the $O_3$(v) has been deactivated.

It is not so easy to determine which of the remaining two pseudo-first-order rate constants should be identified with reaction 3, or with reaction 4. One approach is to express the fitted reaction rate constants as pseudo-second-order rate constants: $k_i{}^{II} = k_i{}^{I}/[O_2]$. For the recombination reaction, $k_3{}^{II} = k_3[O_2]$ is directly proportional to $[O_2]$, whereas for vibrational deactivation, $k_4{}^{II} = k_4$ is constant. Therefore, a plot of the pseudo-second-order rate constants as functions of pressure is expected to give two straight lines: one that is proportional to oxygen pressure and one that is independent of pressure.[41] All of the experimental data (more than 40 runs) were analyzed in this way and the results are shown in Figure 5. The lines show the behavior expected from the two reactions. The fastest pseudo-first-first-order rate constant corresponds to reaction 4 at pressures lower than about 700 Torr, but, at higher pressures, the fastest process corresponds to reaction 3: there is a switch at ~700 Torr in the identity of the process responsible for the rising portion of the experimental IRF curves.

The data points deviate dramatically from the expected straight lines. The deviations are mostly due to the effects of experimental noise, which creates correlations between the rate constants.[41] An important consequence of the deviations of the data points from the expected straight lines is that the lower branch of data points (Figure 5), which one might associate with reaction 3, follows a curved line. This behavior caused Shi and Barker[10] to conclude erroneously that excited electronic states may play a role in the O + $O_2$ recombination reaction.

A more sophisticated statistical analysis is needed in order to extract all of the information that can be recovered from the experimental data.

**$\chi^2$ Analysis.** This type of statistical analysis shows explicitly the correlations among parameters and helps in determining the parameter values and associated uncertainties. The $\chi^2$ function is the same as that used in ordinary least squares:

$$\chi^2 = \sum_{i=1}^{N}\left[\frac{(y_i - y_i^{\mathrm{exp}})}{\sigma_i}\right]^2 \tag{13}$$

where $y_i$ and $y_i{}^{\mathrm{exp}}$ are the fitted and experimental values, respectively, of an observable, and $\sigma_i{}^2$ is the variance for the $i$th data point, for a total of $N$ data points. In this analysis, the average variance $(\sigma_i{}^2)$ per datum was obtained from the pretrigger data for each experimental run. The pre-trigger data (not shown in the figures) comprised ~20% of the data set for each experimental run. Moreover, the noise from the infrared detector did not appear to depend on signal amplitude.

The $\chi^2$ analysis was carried out by constructing a $\chi^2$ surface, as follows.[42] The analytical expression obtained for $[O_3(v)]$ (eq 7) was used to fit the experimental data. For the $\chi^2$ projection on the $(k_3,k_4)$ plane, $k_3$ and $k_4$ were given assigned values and the remaining parameters were then optimized via nonlinear least squares of the *combined* data set (consisting of all 43 experimental data sets) in order to minimize $\chi^2$. By varying the assigned values of $k_3$ and $k_4$, a $\chi^2$ surface was constructed: $\chi^2(k_3,k_4)$.

A contour plot of $\chi^2(k_3,k_4)$ is presented in Figure 6 along with $\chi^2$ surfaces for some of the other parameter pairs. The contours are at intervals of $\Delta\chi^2 = 1$ and the minimum numerical value of $\chi^2$ for each plot is shown in the vicinity of the

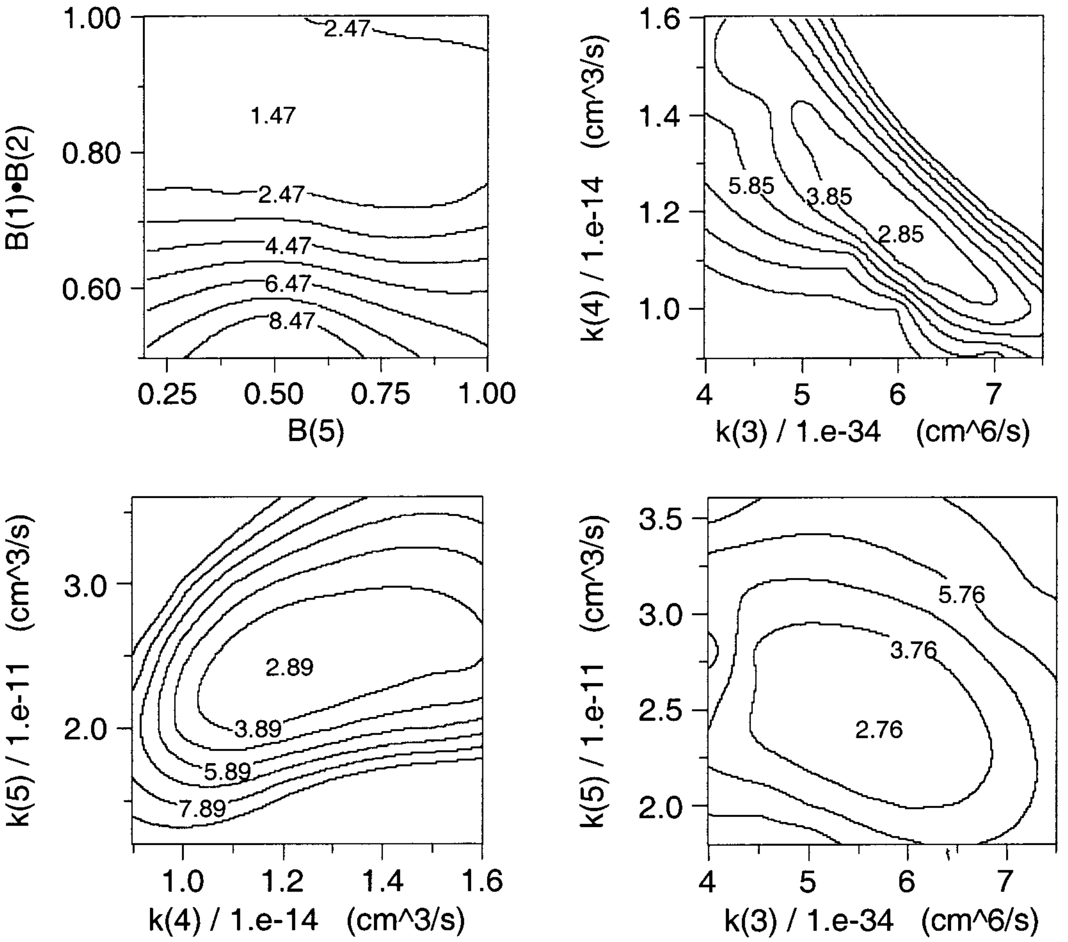

**Figure 6.** $\chi^2$ projections for pairs of parameters. See text for details.

minimum. The minimum numerical value of $\chi^2$ is expected to be ~2, because two degrees of freedom are fixed in each plot, while the other degrees of freedom are fitted via nonlinear least squares.[42] In each case, the minimum numerical value of $\chi^2$ is of the correct order, indicating that the estimates for $\sigma_i^2$ are reasonable. Representative fits corresponding to the minimum in $\chi^2(k_3,k_4)$ are shown as solid lines in Figure 2.

The $\chi^2$ contour plot for the branching ratios shows that any value of $B_5$ from zero to unity is consistent with the experimental data; other contour plots involving $B_5$ (not shown) are also consistent with this conclusion. The lack of sensitivity to $B_5$ is because $O_3(v)$ is produced via both channels of reaction 5: reaction 5a yields O-atoms, which react very rapidly via reaction 3 to produce $O_3(v)$, and reaction 5b produces $O_3(v)$ directly. The minimum value for $\chi^2$ occurs where $B_1 \times B_2 = 0.86$ and $B_5 = 0.61$. The experimental uncertainties associated with these quantities are obtained from the projections of the $\Delta\chi^2 = 1$ contour (68% confidence) on the corresponding axis. For branching ratio $B_5$, the $\Delta\chi^2 = 1$ contour extends beyond $B_5 = 0$ and 1 when $B_1 \times B_2 = 0.86$. Thus we conclude that experiments are insensitive to $B_5$. When $B_5 = 0.61$, the projections of the $\Delta\chi^2$=1 contour give 68% confidence limits of $B_1 \times B_2 = 0.73$ and 0.99. Thus we conclude that $B_1 \times B_2 = 0.86 \pm 0.13$ (68% confidence limits). If we adopt the literature value $B_1 = 0.91 \pm 0.03$ at 248 nm, then $B_2 = 0.95^{+0.05}{}_{-0.13}$. This result is consistent with 0.77 ± 0.23, reported by Lee and Slanger,[43] and 0.8, reported by Amimoto and Wiesenfeld,[44] but the uncertainty has been reduced significantly.

The $\chi^2$ projection plots for the other parameter pairs were analyzed in the manner described in the preceding paragraphs. Each rate constant can be used in several different $\chi^2$ projection plots and thus it is possible to deduce slightly different values for the rate constant and associated uncertainties, depending on the choice of the projection. The deduced values for the parameters are presented in Table 1.

**TABLE 1: Summary of Results**

| parameter | values | notes | references |
|---|---|---|---|
| $B_1 \times B_2 = \dfrac{k_{1a}k_{2a}}{k_1k_2}$ | 0.86 ± 0.13 | a, e | this work |
| $B_2 = k_{2a}/k_2$ | 0.8 | g | 44 |
| $B_2 = k_{2a}/k_2$ | 0.77 ± 0.23 | | 43 |
| $B_2 = k_{2a}/k_2$ | 0.95 (+0.05/−0.13) | a, b, e | this work |
| $k_3/10^{-34}$ cm$^6$ s$^{-1}$ | 6.0 ± 0.7 | c | 1 |
| $k^3/10^{-34}$ cm$^6$ s$^{-1}$ | 6.0 ± 1.1 | a, c, e | this work |
| $k_4/10^{-14}$ cm$^3$ s$^{-1}$ | 1.2 ± 0.2 | a, d, e | this work |
| $k_5/10^{-11}$ cm$^3$ s$^{-1}$ | 2.2 ± 0.4 | | 2 |
| $k_5/10^{-11}$ cm$^3$ s$^{-1}$ | 2.4 ± 0.5 | a, e | this work |
| $k_5/10^{-11}$ cm$^3$ s$^{-1}$ | 2.26 ± 0.15 | a, f<br>(recommended) | this work |

[a] 68% confidence interval. [b] Assuming[35] $B_1 = 0.91 \pm 0.03$ at 248 nm. [c] For $O_2$ as third body. [d] Measured at 9.6 $\mu$m. [e] From $\chi^2$ projections (Figure 6). [f] From least-squares analysis (Figure 4). [g] Uncertainty was not specified.

In Figure 6, the $\chi^2$ plots show that rate constant $k_5$ is not strongly correlated with $k_3$ and $k_4$, but rate constants $k_3$ and $k_4$ are strongly (anti)correlated with each other. Rate constant $k_5$ is not strongly correlated with the others because its magnitude is much smaller: the time scales are widely separated. This result is consistent with the high quality of the nonlinear least-squares fit shown in Figure 4. In fact, we recommend the nonlinear least squares result: $k_5 = (2.26 \pm 0.04) \times 10^{-11}$ cm$^3$ s$^{-1}$. The estimated measurement errors are of the order of ±5%

**TABLE 2: Additional Parameters Needed for Simulations**

| parameter | value | reference |
|---|---|---|
| $k_2$ | $4 \times 10^{-11}$ cm$^3$ s$^{-1}$ | 2 |
| $B_5$ | 0.55 | this work |
| $k_6$ | $3.9 \times 10^{-7}$ cm$^3$ s$^{-1}$ | 2 |

and thus the recommended rate constant is $k_5 = (2.26 \pm 0.15) \times 10^{-11}$ cm$^3$ s$^{-1}$. Rate constants $k_3$ and $k_4$ are strongly (anti)-correlated because the corresponding pseudo-first-order rate constants are of the same order in the experiments and thus the time scales are not widely separated. Indeed, $k_3^{\mathrm{I}}$ is greater than $k_4^{\mathrm{I}}$ in some of the experimental runs, but the opposite is true in others (see Figure 5). Even in the presence of only modest amounts of experimental noise, the rate constants cannot be obtained without significant correlation.

Simulations of some experiments were carried out to determine whether the results in Table 1 combined with data from the literature can accurately describe the experimental IRF data. The model consisted of the recommended results summarized in Table 1 and values for several other parameters, as listed in Table 2. Note that the results are not sensitive to branching ratio $B_5$ and a value near $B_5 = 0.7$ would give the same results. The differential equations were solved numerically using the Gear algorithm and the results were in good agreement with the experimental data. We also carried out simulations that included additional minor reactions (e.g., O + $O_3$, O($^1$D) + $O_3$, $O_2(^1\Delta_g)$ + $O_2$, $O_2(^1\Delta_g)$ + $O_3$, $O_2(^1\Delta_g)$ + $O_2(^1\Delta_g)$), but the simulations were almost identical with the simpler mechanism. Thus we conclude that the minor reactions do not contribute significantly and the analytical model gives an accurate representation of the experimental data.

## Discussion

The results of the present work described in Table 1 are in good agreement with previous investigations, which used different techniques and which usually employed much more limited ranges of $O_2$ pressure. As indicated above, the time constant for reaction 5 was well separated from the others under the present experimental conditions, enabling us to deduce the rate constant with high precision. The result is in excellent agreement with other studies. Because the time constants for reactions 3 and 4 were so similar, the two rate constants exhibited strong (anti)correlation due to the effects of experimental noise. Nonetheless, the deduced rate constants are in good agreement with previous results, although the resulting uncertainties are larger in the present work. The branching ratio for reaction 2 was not greatly affected by correlations and it was possible to determine this quantity more precisely than in previous work.

The good agreement of the present results with previous investigations supports the conventional mechanism that was used in the analysis. The anomalous pressure dependence of reaction 3 reported by Shi and Barker[10] can now be explained as being due to the effects of correlation among rate constants, and not as being due to ozone excited electronic states. It is possible that some of the anomalies reported in other investigations may have been due to these effects.

The new value for branching ratio $B_2 = 0.95$ (+0.05/−0.13) may have a significant impact on studies that use airglow in the atmospheric bands to deduce O($^1$D) concentrations.[22,23] This value is not significantly different from unity and it indicates that reaction 2a is strongly favored, compared to reaction 2b.

Reaction 4 summarizes a complicated process, which has been modeled by several groups.[11−13,30,38,45] The models indicate that highly vibrationally excited $O_3$(v) is deactivated in a sequential process in which the stretching vibrations, which have similar frequencies, are deactivated at a rate different from that of the bending vibration. The models predict that the transition from (0 1 0) to (0 0 0) is the final step in the sequence. Rate constant $k_4$ found in the present work is only about half as large as the known rate constant[38,39] for this final step, showing that the global rate is controlled by the whole cascade down the energy ladder and not solely by the final step.

Although we will present only a qualitative description here, we constructed[46,47] a detailed model of state-to-state energy transfer in ozone and compared it to the detailed IRF data, such as that shown in Figure 2. The model was constructed by using SSH(T) theory[48−50] in a semiempirical mode. The theoretical parameters were adjusted[51,52] in order to force the SSH(T) state-to-state rate constants to match those known from experiment for the lowest vibrational states. The theory was then used to calculate the most important rate constants linking virtually all of the ozone vibrational states and, to simplify the model, some of the states were grouped. The system of differential equations resulting from this model was solved numerically[53] using the Gear algorithm for stiff differential equations in order to ascertain time-dependent species concentrations. Einstein coefficients for spontaneous emission were estimated[29] and used with the species concentrations to estimate IRF intensity, which was convoluted with the instrument response function to simulate an IRF experiment.

The resulting simulations were virtually indistinguishable from the experimental data, showing that the vibrational deactivation model is at least plausible. Furthermore, the model reproduced the decay rate associated with reaction 4, even though the individual state-to-state rate constants are somewhat faster. The slower rate is the result of the multiple-step energy cascade.

Although this model is plausible, it is not unique, because there are several ways that the theoretical parameters can be adjusted in order to match experiments. Moreover, SSH(T) theory suffers from well-known defects and its predictions, semiempirical or otherwise, are not known to be reliable. For these reasons, no further details are presented here.

## Conclusions

The principal conclusion from this work is that the results can be explained using a conventional mechanism without the need for invoking excited electronic states of ozone. However, excited electronic states of oxygen atoms and oxygen molecules play important roles in the system. Because of this, it was possible to obtain with high precision rate constant $k_5$ for the quenching of $O_2(^1\Sigma_g^+)$ by ozone and branching ratio $B_2$ for the production of $O_2(^1\Sigma_g^+)$ from the quenching of O($^1$D) by $O_2$. Rate constants for the O + $O_2$ reaction and the deactivation of $O_3$(v) were also obtained, but with more uncertainty, due to the effects of experimental noise. It is possible that the noise and slow detector response times are responsible for anomalous results reported in other studies.

**Acknowledgment.** Thanks for funding go to NSF (Atmospheric Chemistry Division) and NASA (Upper Atmosphere Research Program). Thanks go to Dr. Ralph E. Weston, Jr., and Brookhaven National Laboratory for the lending us the infrared detector we designated as HCT-2. We also thank Prof. Stanley J. Jacobs for helpful discussions. J.R.B. thanks Prof. William L. Hase and the Chemistry Department at Wayne State University for their hospitality during a sabbatical visit.

## References and Notes

(1) Atkinson, R.; Baulch, D. L.; Cox, R. A.; Hampson, R. F.; Kerr, J. A.; Rossi, M. J.; Troe, J. *J. Phys. Chem. Ref. Data* **1997**, *26*, 1329−499.

(2) DeMore, W. B.; Sander, S. P.; Golden, D. M.; Hampson, R. F.; Kurylo, M. J.; Howard, C. J.; Ravishankara, A. R.; Kolb, C. E.; Molina, M. J. *Chemical Kinetics and Photochemical Data for Use in Stratospheric Modeling*. Evaluation Number 12; Jet Propulsion Laboratory: Pasadena, CA, 1997; Vol. 97-4.

(3) Steinfeld, J. I.; Adler-Golden, S. M.; Gallagher, J. W. *J. Phys. Chem. Ref. Data* **1987**, *16*, 911−51.

(4) Wayne, R. P. *Atmos. Environ.* **1987**, *21*, 1683−1694.

(5) Locker, J. R.; Joens, J. A.; Bair, E. J. *J. Photochem.* **1987**, *36*, 235−45.

(6) Kleindienst, T.; Locker, J. R.; Bair, E. J. *J. Photochem.* **1980**, *12*, 67−74.

(7) von Rosenberg, C. W.; Trainor, D. W. *J. Chem. Phys.* **1974**, *61*, 2442−56.

(8) von Rosenberg, C. W.; Trainor, D. W. *J. Chem. Phys.* **1975**, *63*, 5348−53.

(9) Hippler, H.; Rahn, R.; Troe, J. *J. Chem. Phys.* **1990**, *93*, 6560−9.

(10) Shi, J.; Barker, J. R. *J. Phys. Chem.* **1990**, *94*, 8390−3.

(11) Rawlins, W. T. *J. Geophys. Res.* **1985**, *90*, 12283−92.

(12) Rawlins, W. T.; Armstrong, R. A. *J. Chem. Phys.* **1987**, *87*, 5202−8.

(13) Rawlins, W. T.; Caledonia, C. E.; Armstrong, R. A. *J. Chem. Phys.* **1987**, *87*, 5209−21.

(14) Adler-Golden, S. M.; Matthew, M. W.; Smith, D. R.; Tatkowski, A. J. *J. Geophys. Res.* **1990**, *95*, 15243−8.

(15) Solomon, S.; Kiehl, J. T.; Kerridge, B. J.; Remsberg, E. E.; Russell, J. M. *J. Geophys. Res.* **1986**, *91*, 9865−76.

(16) Mlynczak, M. G.; Drayson, S. R. *J. Geophys. Res.* **1990**, *95*, 16497−511.

(17) Mlynczak, M. G.; Drayson, S. R. *J. Geophys. Res.* **1990**, *95*, 16513-21.

(18) Fichet, P.; Jevais, J. R.; Camy-Peyret, C.; Flaud, J. M. *Planet. Space Sci.* **1992**, *40*, 989−1009.

(19) Mlynczak, M. L. *J. Geophys. Res.* **1991**, *96*, 17217−28.

(20) Mlynczak, M. L.; Solomon, S. *J. Geophys. Res.* **1993**, *98*, 10517−42.

(21) Mlynczak, M. L.; Zhou, D. K. *Geophys. Res. Lett.* **1998**, *25*, 639.

(22) Brasseur, G.; Solomon, S. *Aeronomy of the Middle Atmosphere*, 2nd ed.; D. Reidel Publishing company: Dordrecht, 1986.

(23) Marsh, D. R.; Skinner, W. R.; Yudin, V. A. *Geophys. Res. Lett.* **1999**, *26*, 1369−72.

(24) Shi, J.; Barker, J. R. *Int. J. Chem. Kinet.* **1990**, *22*, 1283−301.

(25) Arnold, D. W.; Xu, C.; Kim, E. H.; Neumark, D. M. *J. Chem. Phys.* **1994**, *101*, 912−22.

(26) Anderson, S. M.; Mauersberger, K. *J. Geophys. Res.* **1995**, *100*, 3033−48.

(27) Barbe, A.; Secroun, C.; P. Jouve. *J. Mol. Spectrosc.* **1974**, *49*, 171.

(28) Flaud, J.-M.; Camy-Peyret, C.; Rinsland, C. P.; Smith, M. A. H.; Devi, V. M. *Atlas of Ozone Spectral Parameters from Microwave to Medium Infrared*; Academic Press Inc.: Boston, 1990.

(29) Adler-Golden, S. M.; Langfoff, S. R.; Bauschlicher, C. W.; Carney, G. D. *J. Chem. Phys.* **1985**, *83*, 255−64.

(30) Upschulte, B. L.; Green, B. D.; Blumberg, W. A. M.; Lipson, S. J. *J. Phys. Chem. A* **1994**, *98*, 2328−36.

(31) Slanger, T. G.; Jusinski, L. E.; Black, G.; Gadd, G. E. *Science* **1988**, *241*, 945−50.

(32) Shi, J.; Barker, J. R. *J. Geophys. Res.* **1992**, *97*, 13039−50.

(33) Bao, Z.-C.; Yu, W. O.; Barker, J. R. *J. Chem. Phys.* **1995**, *103*, 6−13.

(34) Yoshino, K.; Esmond, J. R.; Murray, J. E.; Parkinson, W. H.; Thorne, A. P.; Learner, R. C. M.; Cox, G. *J. Chem. Phys.* **1995**, *103*, 1243−9.

(35) Wine, P. H.; Ravishankara, A. R. *Chem. Phys.* **1982**, *69*, 365−73.

(36) Rawlins, W. T.; Murphy, H. C.; Caledonia, G. E.; Kennealy, J. P.; Robert, F. X.; Corman, A.; Armstrong, R. A. *Appl. Opt.* **1984**, *23*, 3316−24.

(37) Menard, J.; Doyennette, L.; Menard-Bourcin, F. *J. Chem. Phys.* **1992**, *96*, 5773−80.

(38) Menard-Bourcin, F.; Doyennette, L.; Menard, J. *J. Chem. Phys.* **1994**, *101*, 8636−45.

(39) Zeninari, V.; Tikhomirov, B. A.; Ponomarev, Y. N.; Courtois, D. *J. Chem. Phys.* **2000**, *112*, 1835−43.

(40) Bevington, P. R. *Data Reduction and Error Analysis for the Physical Sciences*; McGraw-Hill: New York, 1969.

(41) Bevan, P. L. T.; Johnson, G. R. A. *J. Chem. Soc., Faraday I* **1973**, *69*, 216−27.

(42) Press: W. H.; Teukolsky, S. A.; Vetterling, W. T.; Flannery, B. P. *Numerical Recipes in FORTRAN. The Art of Scientific Computing*, 2nd ed.; Cambridge University Press: Cambridge, 1992.

(43) Lee, L. C.; Slanger, T. G. *J. Chem. Phys.* **1978**, *69*, 4053−60.

(44) Amimoto, S. T.; Wiesenfeld, J. R. *J. Chem. Phys.* **1980**, *72*, 3899−3903.

(45) Menard-Bourcin, F.; Boursier, C.; Doyennette, L.; Menard, J. *J. Phys. Chem.* **1996**, *100*, 15015−20.

(46) Shi, J. Photochemical kinetics of excited states of $O_3$ and $O_2$: Laboratory studies and atmospheric implications. Ph.D. Dissertation, University of Michigan, Ann Arbor, 1991.

(47) Green, J. G.; Barker, J. R. Unpublished calculations, 1999.

(48) Schwartz, R. N.; Slawsky, Z. I.; Herzfeld, K. F. *J. Chem. Phys.* **1952**, *20*, 1591.

(49) Herzfeld, K. F.; Litovitz, T. A. *Absorption and Dispersion of Ultrasonic Waves*; Academic Press: New York, 1959.

(50) Tanczos, F. I. *J. Chem. Phys.* **1959**, *30*, 1119.

(51) Barker, J. R. Stalking the Step-size Distribution: A Statistical-Dynamical Theory for Large Molecule Collisional Energy Transfer. In *Highly Excited States: Relaxation, Reaction, and Structure*; Mullin, A., Schatz, G. C., Eds.; American Chemical Society: Washington, DC, 1997; Vol. 678, pp 220−236.

(52) Barker, J. R. *Ber. Bunsen-Ges. Phys. Chem.* **1997**, *101*, 566.

(53) Whitten, G. Z.; Hogo, H. Science Applications Inc., 1980.

(54) Fink, E. H.; Setzer, K. D.; Wildt, J.; Ramsay, D. A.; Vervloet, M. *Int. J. of Quant. Chem.* **1991**, *39*, 287.